



The Interplay of Demographic Variables and Social Distancing Scores in Deep Prediction of U.S. COVID-19 Cases

Francesca Tang^{*a}, Yang Feng^{*b}, Hamza Chiheb^c, and Jianqing Fan^a

^aDepartment of Operations Research and Financial Engineering, Princeton University, Princeton, NJ; ^bDepartment of Biostatistics, New York University, New York City, NY; ^cNew York City, NY

ABSTRACT

With the severity of the COVID-19 outbreak, we characterize the nature of the growth trajectories of counties in the United States using a novel combination of spectral clustering and the correlation matrix. As the United States and the rest of the world are still suffering from the effects of the virus, the importance of assigning growth membership to counties and understanding the determinants of the growth is increasingly evident. For the two communities (faster versus slower growth trajectories) we cluster the counties into, the average between-group correlation is 88.4% whereas the average within-group correlations are 95.0% and 93.8%. The average growth rate for one group is 0.1589 and 0.1704 for the other, further suggesting that our methodology captures meaningful differences between the nature of the growth across various counties. Subsequently, we select the demographic features that are most statistically significant in distinguishing the communities: number of grocery stores, number of bars, Asian population, White population, median household income, number of people with the bachelor's degrees, and population density. Lastly, we effectively predict the future growth of a given county with a long short-term memory (LSTM) recurrent neural network using three social distancing scores. The best-performing model achieves a median out-of-sample R^2 of 0.6251 for a four-day ahead prediction and we find that the number of communities and social distancing features play an important role in producing a more accurate forecasting. This comprehensive study captures the nature of the counties' growth in cases at a very micro-level using growth communities, demographic factors, and social distancing performance to help government agencies utilize known information to make appropriate decisions regarding which potential counties to target resources and funding to. Supplementary materials for this article, including a standardized description of the materials available for reproducing the work, are available as an online supplement.

ARTICLE HISTORY

Received January 2021
Accepted March 2021

KEYWORDS

Block model; Community detection; COVID-19; Learning; Neural network; Spectral clustering; Stochastic machine



1. Introduction

The recent infectious disease (COVID-19) caused by severe acute respiratory syndrome coronavirus 2 (SARS-CoV-2) has overtaken the world as the largest pandemic we have seen in decades. The World Health Organization (WHO) labeled it a pandemic on 03/11/2020, with a total of more than 110 million confirmed cases and more than 2.44 million deaths worldwide as of 02/20/2021.


Forecasting the growth of confirmed cases and the locations of future outbreaks has been a persistent challenge in the public health and statistical fields. With the gravity and urgency of the global health crisis, many recent works including Kucharski et al. (2020) and Peng et al. (2020) have attempted to model the growth in cases in various countries. Most of the literature on statistical modeling of the data focuses on the reproduction number. However, this value is constantly evolving and is not always a valuable measurement to build prediction models with. Hong and Li (2020) proposed a Poisson model with time-dependent transmission and removal rates to estimate a time-dependent disease reproduction number. Betensky and Feng (2020) studied the impact of incomplete testing on the estimation of dynamic doubling time. Ultimately, we need to


examine the underlying features contained in the time series data in order to extract valuable insights into the unique nature of the spread of COVID-19. As the number of deaths is at least a two-week lagging indicator compared to the number of confirmed cases, we only look at the latter. More importantly, the matrix of the number of deaths per county would be very sparse at the initial stage, making any analysis more difficult. Our goal is to first characterize and categorize the disease progression of various counties given the limitations of public data. Then after distinct growth communities are found, the demographic variables and social distancing scores are incorporated to project the future behavior of the growth curve. In this way, a holistic outlook can be gleaned of the pandemic on a granular level, while maintaining accuracy and robustness.

Stochastic block models (SBMs), first developed by Holland, Laskey, and Leinhardt (1983), have long been studied as a powerful statistical tool in community detection, where the nodes or members are partitioned into latent groups. SBMs have been employed to study social networks (Wasserman and Anderson 1987), brain connectivity (Rajapakse, Gupta, and Sui 2017), protein signaling networks (Chen and Yuan 2006), and many other applications. Under an SBM, the nodes within the same group

CONTACT Yang Feng  yang.feng@nyu.edu  Department of Biostatistics, New York University, New York City, NY 10012.

*Tang and Feng contribute equally to this work.

 Supplementary materials for this article are available online. Please go to www.tandfonline.com/r/JASA.

 These materials were reviewed for reproducibility.

© 2021 American Statistical Association

usually have a higher probability of being connected versus those from different groups. The difficult task is to recover these connectivities and the communities based on one observation, which in our case, is a snapshot of the changes in the number of cases up to the most recent time point. In more recent years, spectral clustering (Balakrishnan et al. 2011; Rohe, Chatterjee, and Yu 2011; Jin 2015; Lei and Rinaldo 2015) has arisen as one of the most popular and widely studied approaches to recover these communities. Conventional spectral clustering algorithms mostly involve two steps: eigen-decompose the adjacency or Laplacian matrix of the data and then apply a clustering algorithm, such as k-means, to the eigenvectors that correspond to the largest or smallest eigenvalues. There is extensive literature on such procedures, for instance, von Luxburg (2007), Ng, Jordan, and Weiss (2001), Abbe (2017), and Chen et al. (2020).

In this study, we introduce the unique procedure of conducting spectral clustering on the sample Pearson correlation coefficient matrix directly and compare its clusters to the standard Laplacian embedding. This complements Brownlees, Gudmundsson, and Lugosi's (2020) approach based on a latent covariance model on financial return data. Gilbert et al. (2020) used agglomerative clustering, an unsupervised learning method, on preparedness and vulnerability data in African countries using self-reported reports of capacity and indicators. While a comprehensive study, it only considers the possible exposures to travelers from China. Using a different dataset, Hu et al. (2020) clustered the data from China by implementing a simple *k*-means clustering directly on various features of the provinces/cities and not on the eigenvectors of the correlation matrix. It also does not take into account possible explanatory features that are not directly related to the number of cases and fails to predict provinces that have yet to have cases. The data processing of some existing approaches also does not standardize and shift the data in a way that aligns with the nature of COVID-19.

Once the communities are found, the subsequent part uncovers the statistically significant demographic features, pre-existing in the counties, that could largely explain a county's community membership. Most of the existing research on salient demographic information focuses on age-related features and the presence of co-morbidities or underlying health conditions, for example, Dowd et al. (2020) and Lippi et al. (2020). In reality, what influences how the disease progresses in a county is most likely a confluence of variables, and not one or two prevailing ones. Some studies also examine how various demographic determinants affect how well a county carries out social distancing (Im et al. 2020), but offers little or no connection to the nature of the growth curve.

There have been several early studies that predict, estimate, or model the growth curve of the disease, including Fanelli and Piazza (2020) on the cases in Italy, France, and China, where the authors claim from pandemic data of the first two months that the mortality rate in Italy is around 3%–7% and 1%–3% in China. Another example is Roda et al. (2020) who used the cases in Wuhan to conclude that an SIR model, a simpler epidemic compartmental model, is superior to an SEIR model, a more complex compartmental model. In addition, Liu et al. (2020) presented a system of ordinary differential equations to model the cases in China, assuming a constant transmission

rate. In addition, deep learning has been applied to COVID-19 research, such as Wang and Wong (2020) that detect positive cases through chest scans. Other studies such as Zheng et al. (2020) investigated when patients are most infectious by using a deep learning hybrid model and Yang et al. (2020) similarly combined the epidemiological SIR model with an LSTM network. However, there are very few studies that compare different time periods of the pandemic under a statistical lens and integrate other important pieces of the puzzle. Hence, the extracted variables from the feature analysis part are then used in conjunction with time series of social distancing scores from Unacast (2020) to fit a recurrent neural network and to ultimately predict the progression of confirmed cases in a given county. It is important to note that for this prediction section, we use the period from the start of the pandemic until 07/20/2020 as this traces the first large spike in cases in the United States and a subsequent plateau. This gives a long enough time series sample and to include much more recent data would include the second large wave of the pandemic, which is counter to the objective of capturing the growth trajectory of a county's peak and fall. Unacast has created a scoreboard of social distancing measures with mobile device tracking data, where a device is assigned to a specific county based on the location the device spent the most amount of time in. The neural network prediction takes these static, inherent county variables, community membership (the clustering results), and social distancing data to predict the future growth of confirmed cases. Taken together, our paper creates a throughline of the pandemic: historical growth curve of confirmed cases, characterization of this growth via clustering, the significant explanatory demographic features, and finally, social distancing measures that give insight into the nature of the future growth trajectory, as displayed in Figure 1. Table 1

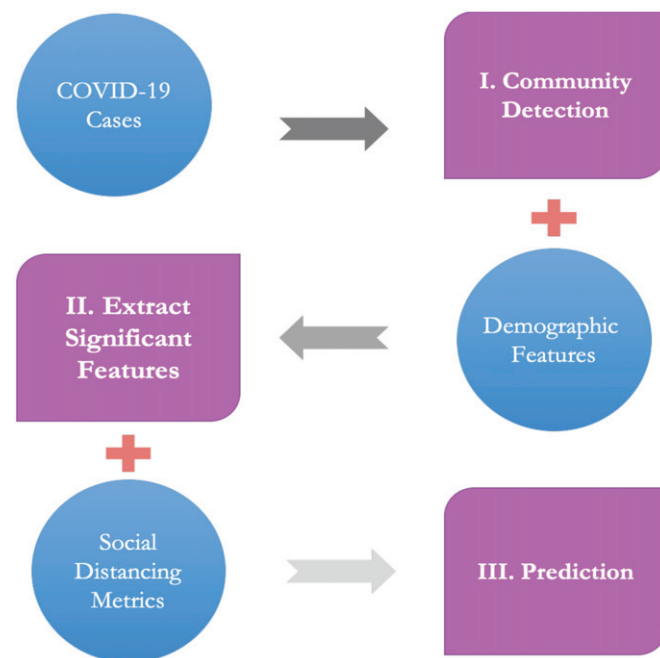


Figure 1. Pipeline of this study's three-part analysis of COVID-19. COVID-19 time series data is first used to perform community detection, clustering counties into several communities. Then, demographic features are incorporated to extract the most significant features that distinguish the growth communities. Finally, social distancing metric time series are added to the results of the previous two parts to carry out the prediction of COVID-19 cases for new counties.

Table 1. Time period, number of counties, and data source used for each part of the article.

	Time period(s)	No. of counties n	Source
Part I	1/22/20–4/17/20 and 5/10/20–7/10/20	950	Johns Hopkins CSSE
Part II	1/22/20–4/17/20 and 5/10/20–7/10/20	633	ACS (c/o Data Planet)
Part III	2/25/20–7/10/20	627	Unacast

also contains the specific time period, the number of counties n , and the data source used for each part of the paper (Part I: community detection, Part II: extraction of significant features, Part III: prediction) as outlined in Figure 1.

2. Community Detection

The first part of this article finds potential communities among the U.S. counties, in which clusters share similar growth patterns, using daily county-level data of the aggregate number of cases. To accomplish this, two fundamental concepts are necessary: the SBM and spectral clustering. The former is a generative model through which community memberships were formed and the latter is a methodology often used to recover these memberships. Compared to traditional clustering methods, spectral clustering has shown to be effective in both statistical and computational efficiency (Abbe 2017; Abbe et al. 2020; Chen et al. 2020). Our approach applies spectral clustering to the correlation matrix, instead of the commonly used adjacency matrix or Laplacian matrix. The goal is to recover the county membership matrix embedded in the correlations of each county's logarithmic daily cumulative number of cases.

2.1. Data

We use the COVID-19 (2019-nCoV) Data Repository by the Johns Hopkins Center for Systems Science and Engineering (CSSE) that contains data on the number of confirmed cases and deaths in the United States and around the world, broken down by counties in the United States. The public database is updated daily and the virtual dashboard is also used widely around the world. Data sources of the database include the World Health Organization (WHO), U.S. Center for Disease Control (CDC), BNO News, Worldometers, and 1point3acres. We take all counties that have 12 or more cumulative cases in the time frame of 01/22/2020 to 04/17/2020. We treat the day a county reaches 12 or more confirmed cases as day one and then discard all counties that have a time series of fewer than 14 days after processing. This way we shift each county to a similar starting point in terms of number of cases and a long enough period to do a meaningful analysis with. We also remove unassigned cases and the U.S. territories, which ultimately results in a total of $n = 950$ counties. Here, we use $w_{i,t} = \log(x_{i,t})$ to represent the logarithmic cumulative cases for county i on day t .

We also repeat the community detection process with more recent data from 05/10/2020, when many states started to reopen, to 07/10/2020. The bulk of this part of the study concentrates on the beginning phase of the pandemic given that

health and government intervention to minimize the number of future cases should be executed as early as possible. However, we compare the resulting communities with more recent data that captures the second phase of the pandemic in the U.S. States experienced a significant drop in cases when the lockdown was enforced and businesses were closed but as they began to reopen, the number of cases saw an uptick once again. Since this second phase comes months after the initial outbreak, there may be meaningful differences worthy of analysis.

2.2. Correlation Matrix vs. Adjacency Matrix

For each county, consider a daily time-series of the cumulative number of confirmed cases, where we use curve registration (the time origin is set as the day on which the number of cases exceeds 12 for a particular county). This curve registration is important as it takes into account the fact that counties may have different COVID-19 outbreak starting times. We denote $w_{i,t} = \log(x_{i,t})$ as the logarithmic cumulative number of cases of county i on the t th day since the county hit 12 or more cases. Then, we use the Pearson correlation as a similarity measure, defined as

$$R_{ij} = \frac{\sum_{t=1}^{T_{ij}} (w_{i,t} - \bar{w}_i)(w_{j,t} - \bar{w}_j)}{\sqrt{\sum_{t=1}^{T_{ij}} (w_{i,t} - \bar{w}_i)^2} \sqrt{\sum_{t=1}^{T_{ij}} (w_{j,t} - \bar{w}_j)^2}}, \quad (1)$$

where $T_{ij} = \min(T_i, T_j)$, with T_i and T_j being the number of days county i and county j has 12 or more cases, respectively. The sample correlation $\mathbf{R} \in \mathbb{R}^{n \times n}$ would then contain the pairwise correlations among all n counties. The logarithmic cumulative case counts are used to align with the exponential growth pattern implied by popular epidemic models. For example, we could distinguish between a faster exponential growth function such as $\exp(2t)$ and a slower growth function $\exp(t/2)$.

Another commonly used network representation is the adjacency matrix \mathbf{A} , which shows whether two counties are connected and is often constructed based on a similarity measure like Pearson correlation or a mutual information score. If the graph is undirected, where each edge that connects two nodes is bidirectional, \mathbf{A} is symmetric. The two most common types of similarity graphs are the ϵ -neighborhood graph and the k -nearest neighbor graph. As we are using sample correlation as the similarity measure, an ϵ -neighborhood adjacency \mathbf{A}_1 is defined as follows:

$$(A_1)_{ij} = \begin{cases} 1, & \text{if } R_{ij} \geq 1 - \epsilon, \\ 0, & \text{otherwise.} \end{cases} \quad (2)$$

A k -nearest neighbor adjacency \mathbf{A}_2 is defined as follows:

$$(A_2)_{ij} = \begin{cases} 1, & \text{if county } i \text{ is among } j\text{'s } k \text{ nearest neighbors} \\ & \text{or if county } j \text{ is among } i\text{'s } k \text{ nearest neighbors,} \\ 0, & \text{otherwise,} \end{cases} \quad (3)$$

where the nearest neighbors are found with respect to R_{ij} .

Depending on the parameters ϵ and k one chooses for \mathbf{A}_1 and \mathbf{A}_2 , respectively, a significant amount of information could be lost in the process because of the thresholding operation. However, this operation also filters out many spurious correlations. Unlike the sparse \mathbf{A}_1 and \mathbf{A}_2 , \mathbf{R} retains all of the pairwise similarities between counties, which would shed more light on the within-group and between-group relationships.

2.3. Stochastic Block Model

The matrices \mathbf{R} , \mathbf{A}_1 , and \mathbf{A}_2 are critical because they can help us recover Θ , an $n \times K$ membership matrix that reflects which community each county belongs to, where K is the number of communities. Letting $Z_i \in \{1, \dots, K\}$ be the community that county i belongs to, the i th row of Θ has exactly one 1 in column Z_i (the community that county i belongs to) and 0 elsewhere. We estimate Θ under an SBM, where the probability two counties are connected only depends on the membership of these two counties. An SBM denoted by $\mathbb{G}(n, \mathbf{B}, \Theta)$ as n nodes, K communities, and is parameterized by Θ and \mathbf{B} , the $K \times K$ symmetric connectivity matrix. Essentially, \mathbf{B} contains the inter- and intra-community connection probabilities: the probability of an edge between counties i and j is B_{Z_i, Z_j} .

The objective is to obtain an accurate estimation $\hat{\Theta}$ of Θ from an observed adjacency matrix \mathbf{A} that is modeled as $\mathbb{G}(n, \mathbf{B}, \Theta)$. This yields a recovery of the partitions $G_k := \{i \in [1, n] : Z_i = k\}$ by $\hat{G}_k = \{i \in [1, n] : \hat{Z}_i = k\}$, $k = 1, \dots, K$, with an ambiguity of permutation of clusters, where \hat{Z}_i indicates the location of 1 in the i th row of $\hat{\Theta}$. The population matrix $\mathbf{P} \in \mathbb{R}^{n \times n}$, where P_{ij} is the probability that counties i and j are connected, is naturally expressed as $\mathbf{P} = \Theta \mathbf{B} \Theta^T$.

2.4. Spectral Clustering

Spectral clustering has been a popular choice for community detection (Rohe, Chatterjee, and Yu 2011; Jin 2015; Lei and Rinaldo 2015). The central idea is to relate the eigenvectors of the observable adjacency matrix \mathbf{A} to those of $\mathbf{P} = \Theta \mathbf{B} \Theta^T$, which is not observed. This is accomplished by expressing \mathbf{A} as a perturbation of its expected value: $\mathbf{A} = \mathbb{E}[\mathbf{A}] + (\mathbf{A} - \mathbb{E}[\mathbf{A}])$. If we treat $\mathbb{E}[\mathbf{A}]$ as the signal part and $\mathbf{A} - \mathbb{E}[\mathbf{A}]$ as the noise, we connect the eigenvectors of \mathbf{A} and \mathbf{P} using $\mathbb{E}[\mathbf{A}] = \mathbf{P} - \text{diag}(\mathbf{P})$. Noting $\text{rank}(\mathbf{P}) = K$, letting $\mathbf{U}_{n \times K} = [\mathbf{u}_1, \dots, \mathbf{u}_K]$ be the eigenspace spanned by the K nonzero eigenvalues of $\mathbb{E}[\mathbf{A}]$, then columns of \mathbf{U} span the same linear space as those spanned by the columns of \mathbf{P} (ignoring $\text{diag}(\mathbf{P})$). Additionally, \mathbf{P} has the same column space as Θ . Now, letting $\hat{\mathbf{U}}$ be the eigenspace corresponding to the K largest absolute eigenvalues of \mathbf{A} , then $\hat{\mathbf{U}}$ is a consistent estimate of \mathbf{U} or the column space of Θ , under some mild conditions. To resolve the ambiguity created by rotation, the k -means algorithm is applied to the normalized rows of \mathbf{U} to identify membership of communities (Rohe, Chatterjee, and Yu 2011; Lei and Rinaldo 2015).

Instead of examining the eigenvalues of \mathbf{A} , spectral graph theory has long studied graph Laplacian matrices as a tool of spectral clustering. The symmetric Laplacian matrix is defined as follows: letting $\mathbf{D} = \text{diag}(d_1, \dots, d_n)$ be the diagonal degree matrix where $d_i = \sum_{j=1}^n A_{ij}$, then a popular definition of a normalized, symmetric Laplacian matrix is $\mathbf{L} = \mathbf{I} - \mathbf{D}^{-1/2} \mathbf{A} \mathbf{D}^{-1/2}$. When clustering with \mathbf{L} , one takes the eigenvectors corresponding to the smallest eigenvalues in absolute value.

In our context, \mathbf{A} can be taken as either \mathbf{A}_1 or \mathbf{A}_2 as outlined in Section 2.2. As there are no exact rules in choosing the parameters ϵ and k of \mathbf{A}_1 and \mathbf{A}_2 , respectively, clustering with \mathbf{L} , which depends on the adjacency matrix, may be less than ideal. It is also an added, often computationally cumbersome

step. Instead, we cluster directly on the similarity matrix \mathbf{R} , the sample correlation matrix. Algorithm 1 delineates the detailed steps of this approach. The classic spectral clustering procedure with \mathbf{L} used as a benchmark is outlined in the supplementary material.

Algorithm 1 Spectral clustering on correlation matrix

Input Sample correlation matrix $\mathbf{R} \in \mathbb{R}^{n \times n}$ and the number of clusters K .

- 1: Compute the top K eigenvectors $\mathbf{u}_1, \dots, \mathbf{u}_K$ of \mathbf{R} associated with top K largest absolute eigenvalues and let $\hat{\mathbf{U}} \in \mathbb{R}^{n \times K}$ be the matrix with the eigenvectors as columns.
- 2: Normalize rows of $\hat{\mathbf{U}}$ to have unit norm to get $\hat{\mathbf{U}}_{\text{norm}}$.
- 3: Cluster the rows of $\hat{\mathbf{U}}_{\text{norm}}$ with k -means.

return Partition $\hat{G}_1, \dots, \hat{G}_K$ of the nodes.

There are several methods for choosing the number of spiked eigenvalues in the context of factor models: scree-plot, eigen-gap, eigen-ratio, adjusted correlation thresholding. As our method involves correlations, we apply the adjusted correlation method in Fan, Guo, and Zheng (2020). This method leads to $K = 2$, which roughly divides the counties into faster or slower growth communities. It also agrees with the choice where we maximize the eigen-gap.

2.5. Clustering Procedure

Figure 2 is a visualization of the first two eigenvectors of \mathbf{R} and the linear separation that the algorithm partitioned all the counties into. The left panel is with unit norm normalization and the right is without the normalization. The result of essentially using the signs of the components of the second eigenvector to cluster reminiscences the work by Abbe et al. (2020) with strong theoretical support. From now on, all clustering analysis will be based on the unit-norm normalization of the eigenvectors.

2.6. Fastest and Slowest Growth Clusters

For future analysis (Section 3), it is useful to define the clusters that contain the counties with the fastest and slowest growth. After the clusters are produced with Algorithm 1, for every community k , we calculate the average exponential growth rates of the counties in that community. This is done by fitting the total number of cases of each county i on day t , $x_{i,t}$, to $x_{i,0}(1 + r_i)^t + \epsilon_{i,t}$ through nonlinear least squares and obtaining the approximated growth rate r_i for county i . Then, we compare the average fitted growth rate $\hat{r}_k = 1/|\hat{G}_k| \sum_{i \in \hat{G}_k} r_i$ and standard error for clusters $k = 1, \dots, K$. The fastest growth cluster is defined as $\text{argmax}_k \hat{r}_k$ and the slowest growth cluster is defined as $\text{argmin}_k \hat{r}_k$.

2.7. Results and Discussion

Table 3 contains information on the average intra- and inter-group correlations, a sample reflection of \mathbf{B} . Evidently, the intra-community correlations are higher than the inter-community correlations. For the first phase, Group 1's intra-correlation of

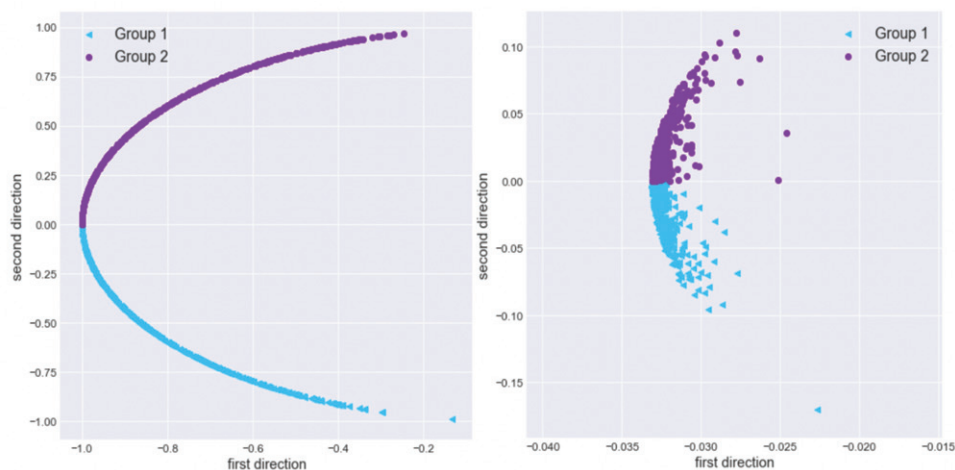


Figure 2. The left panel is the first two unit-norm normalized eigenvectors of R and the corresponding clusters, Group 1 in blue and Group 2 in purple. The right panel depicts the same two clusters but in the two unnormalized eigenvectors.

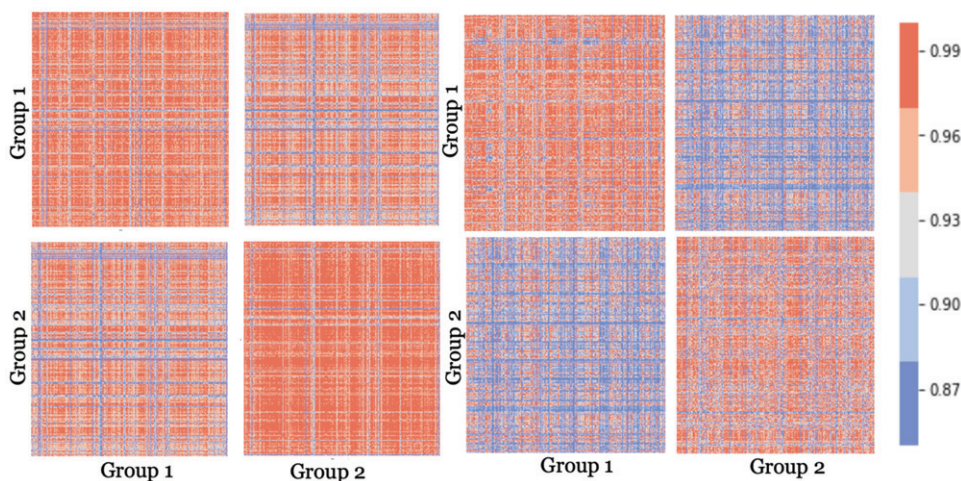


Figure 3. The left panel is the R Heatmap of block correlations $K = 2$ for the first phase 1/22/20 - 4/17/20, corresponding to the left panel of Table 3. The right panel is the R Heatmap of block correlations $K = 2$ for the entire period of study 1/22/20 - 7/10/20, corresponding to the right panel of Table 3. Model R corresponds to Algorithm 1 where we use the sample correlation matrix. Groups 1 and 2 are the obtained partitions \hat{G}_1 and \hat{G}_2 , respectively.

Table 2. Average growth rates and the number of counties in each cluster for $K = 2$.

Model	Group 1			Group 2		
	No. of Counties	Growth Rate	SE	No. of Counties	Growth Rate	SE
R	467	0.1589	0.0020	483	0.1704	0.0019
A_1	462	0.1583	0.0020	488	0.1677	0.0019
A_2	470	0.1605	0.0020	470	0.1664	0.0020
R , second phase	487	0.0207	0.0005	463	0.0233	0.0005

NOTES: Model R corresponds to Algorithm 1 where we use the sample correlation matrix. Model A_1 corresponds to Algorithm 4 where we use the k -nearest neighbors graph ($k = 7$). Model A_2 corresponds to Algorithm 4 where we use the ϵ -neighborhood graph ($\epsilon = 0.007$). Groups 1 and 2 are the obtained partitions \hat{G}_1 and \hat{G}_2 , respectively. Growth Rate is the approximated exponential growth rate, calculated as in Section 2.6. Presented are the averages of these growth rates and their associated SEs for the counties in two groups, clustered by different methods. R , second phase is for the clusters obtained for the period 05/10/2020–07/10/2020.

96.1% and Group 2’s 96.8% are greater than 94.0%, the inter-group correlation between the two groups. As we only took counties with significant outbreaks as of 04/17/2020 and counties have not been fully differentiated yet at an early stage in terms of cases, it is logical to observe high correlations across the board. However, we see that for the entire period of study, the distinction between inter- and intra-community correlations is much more obvious, where the former has decreased significantly. These results are also mirrored in Figure 3, heatmaps of the block correlations.

We can see from Table 2 that for the clusters obtained by Algorithm 1 (R), the difference between the growth rates of Group 1 and Group 2 is the largest. This differentiation is further bolstered by the growth curves in Figures 4 and 5. The standard error bands in Figure 4 underscores that the two groups become more distinct in their growth trajectory as time goes on. For A_1 and A_2 , the growth rates are much closer together between the two communities. Furthermore, the right panel of Figure 5 is a plot of the average cases for the period after community detection was performed: 04/17/2020–09/03/2020. Evidently,

Table 3. The table on the left is the R average block correlations $K = 2$ for the first phase 1/22/20–4/17/20 and the table on the right is the R average block correlations $K = 2$ for the entire period of study 1/22/20–7/10/20.

Group	1	2	Group	1	2
1	96.1%	94.0%	1	95.0%	88.4%
2	94.0%	96.8%	2	88.4%	93.8%

the separation between the two groups becomes much more distinct as time goes on (with a much larger number of cases). As for community detection of the subsequent phase of the pandemic in the United States (from 05/10/2020 to 07/10/2020), the last row of Table 2 again shows a larger average growth rate for Group 2, albeit much smaller in magnitude since cases increased at a slower rate once the country learned how to deal with the pandemic.

Some notable counties that are partitioned to Group 2, the fast growth community, include Los Angeles, CA; San Francisco, CA; District of Columbia; DeKalb, GA; Fulton, GA; Miami-Dade, FL; Cook, IL; Jefferson, LA; Suffolk, MA; Bergen, NJ; New York, NY; Westchester, NY; and King, WA, all large epicenters. Figure 6 is a geographical visualization of the communities.

In addition, Figure 7 shows the same plots as those in Figure 5 but for a later phase. The curves are clearly much flatter in both groups, which is likely due to the increase in the number of cases plateauing in many counties. Furthermore, the distinction between the curves of Group 1 and 2 is also considerably bigger than those of the earlier data. This can be explained by the confluence of additional factors that separate each county’s experience with the virus, including the nature of local government intervention, degree, and timing of re-openings, travel restrictions, etc.

3. Extracting Significant Demographic Features

An important and subsequent question that arises once the communities are obtained is what underlying factors play a role in which growth cluster a county belongs to. Since the growth of COVID-19 cases is also related to static, inherent factors that are not a consequence of the disease, we examine a variety of county demographic variables and how they differ among communities. In order to select the variables that are most statistically significant, or are most relevant to the community assignment of a county, we perform independent two-sample

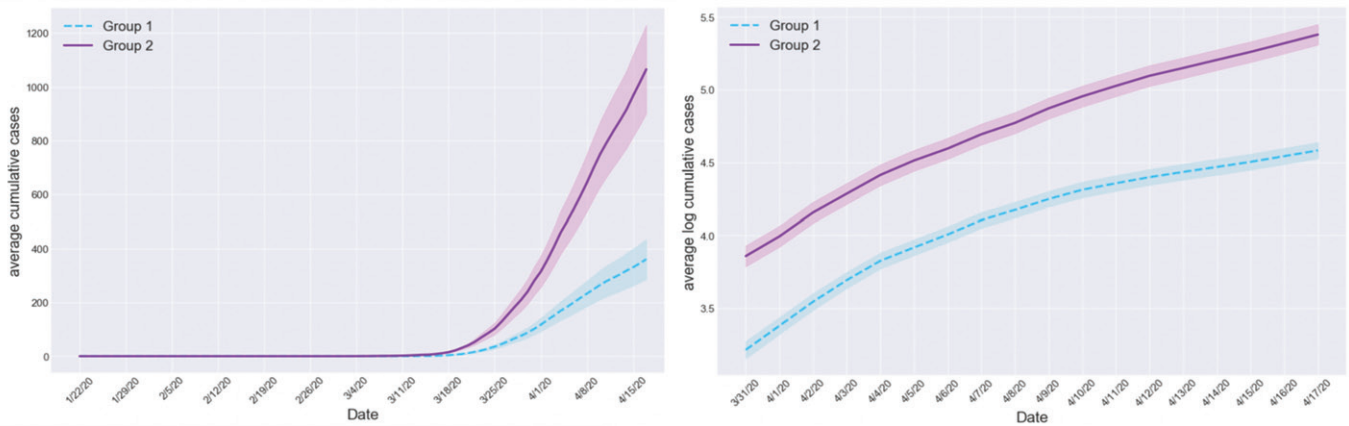


Figure 4. The left panel represents the average cumulative number of cases of the initial phase 01/22/2020 - 04/17/2020 with one standard error bands for the clusters of $R, K = 2$. The right panel is the average log cumulative number of cases of $R, K = 2$. The x-axis is in calendar time, which does not account for heterogeneous starting times of the outbreak in each county.

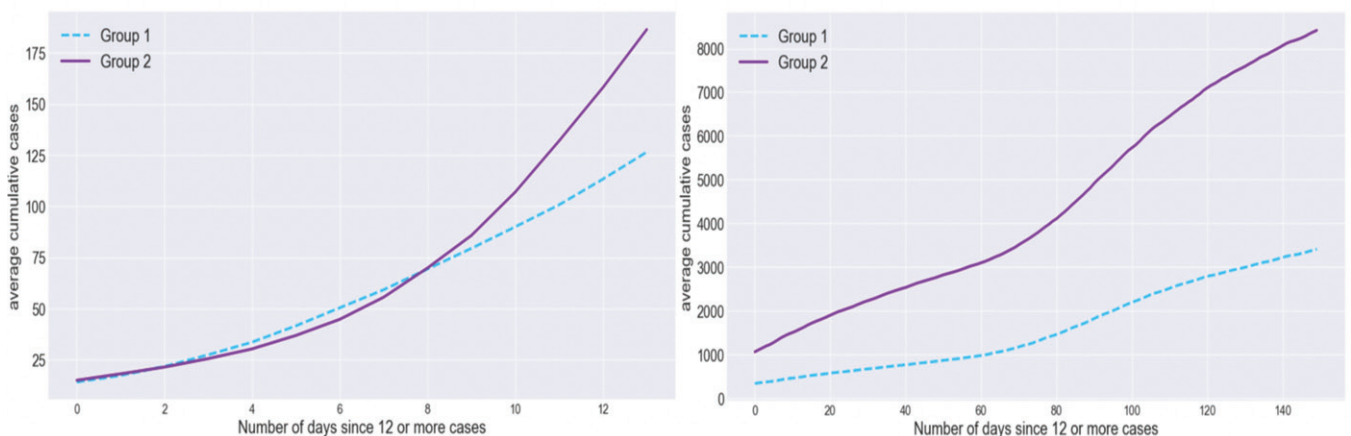


Figure 5. The left panel represents average cumulative number of cases of the initial phase 01/22/2020 - 04/17/2020, starting from the first day of at least 12 days for the clusters of $R, K = 2$. The right panel is the average cumulative number of cases of the period 04/18/2020 - 09/03/2020, the time frame after the initial phase used in community detection. The x-axis here accounts for the heterogeneity of the outbreak of COVID-19 in each county.

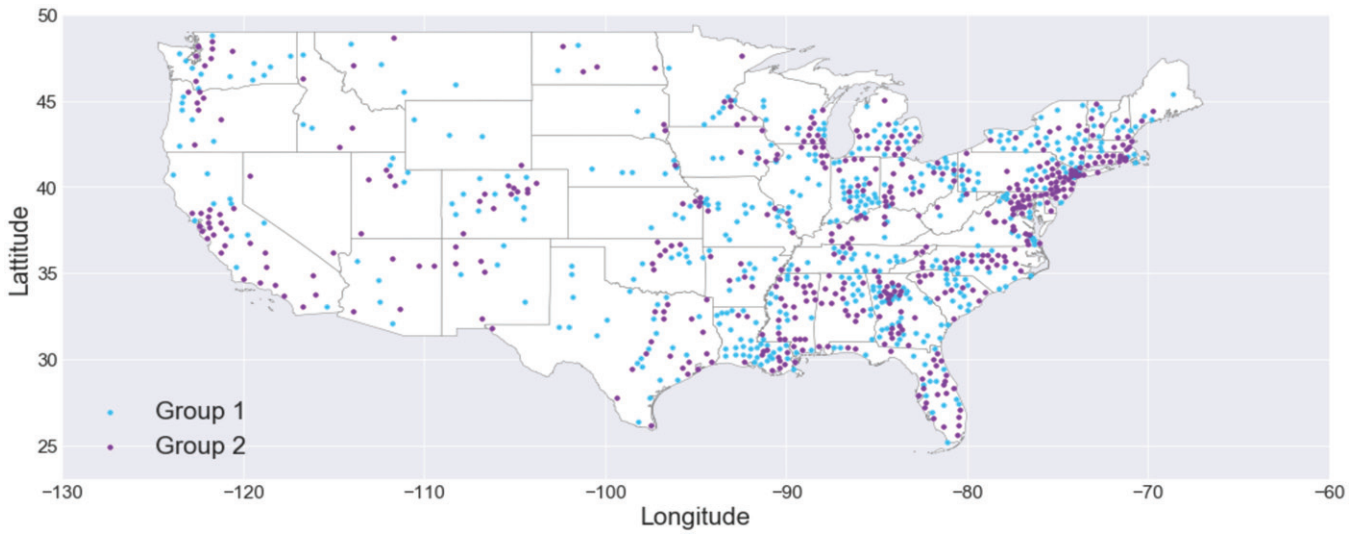


Figure 6. Clusters for model R of the initial phase 01/22/2020 - 04/17/2020. Model R corresponds to Algorithm 1 where we use the sample correlation matrix. Groups 1 and 2 are the obtained partitions \hat{G}_1 and \hat{G}_2 , respectively.

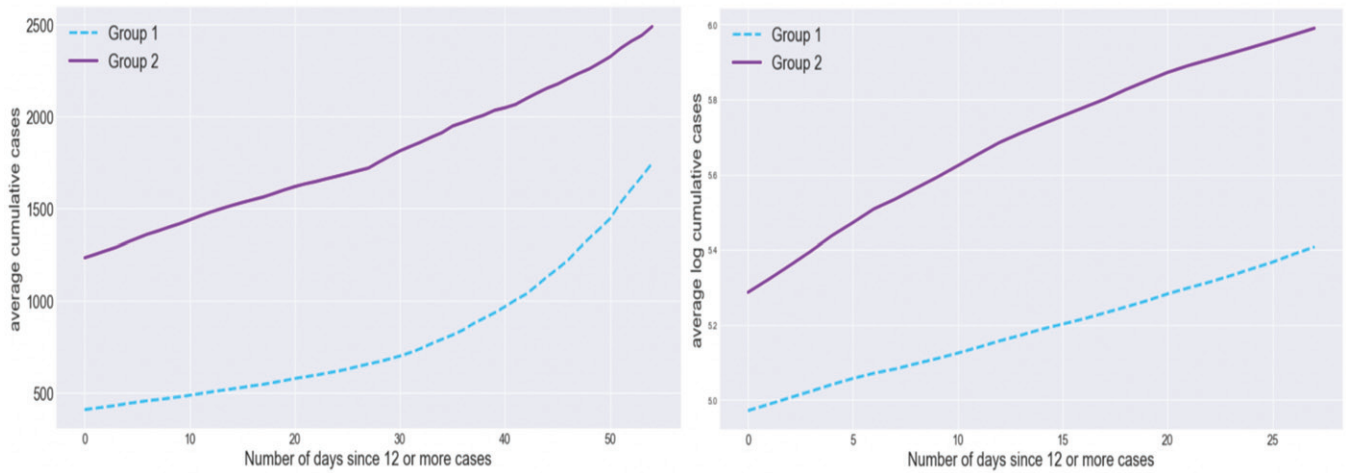


Figure 7. Growth curves of clusters obtained from community detection on data from 05/10/2020 - 07/10/2020 (recent phase). Plots are the same as those of Figure 5.

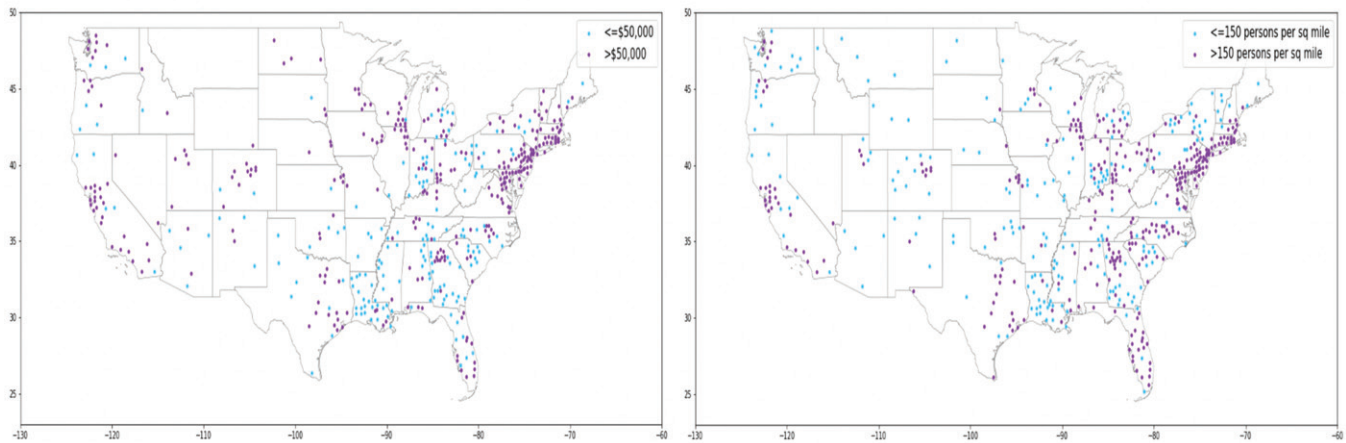


Figure 8. The left panel is a geographical representation of counties according to median household income. Blue dots are counties with less than \$50,000 median annual household income and purple dots are counties with more than \$50,000 median annual household income. The right panel is a geographical representation of counties according to population density. Blue dots are counties with less than 150 persons per sq mile and purple dots counties with more than 150 persons per sq mile.

Table 4. *R* clusters' mean and median values for selected features for each community $K = 2$.

Feature	Group 1			Group 2		
	Mean	Median	Std Dev	Mean	Median	Std Dev
Population density	275.775	159.260	394.059	913.182	289.610	3659.76
Median household income	54431.6	52651.0	13386.3	58814.6	56074.0	16737.2
% Poverty	14.0656	13.3000	5.71511	13.4712	12.5000	5.83384
% 1-person households	27.1330	27.7185	4.21220	27.0233	27.1978	4.54690
% 5 or more person households	8.91332	8.41406	2.96792	9.38467	8.71688	3.27316
% households w 60 y/o and older	39.3294	39.1802	6.85032	38.7538	38.6947	6.03233
% w low access to stores	21.8723	21.3800	9.66507	20.8704	21.2500	9.81211
% low income w low access to stores	7.48273	6.85500	4.48466	6.60216	5.69000	4.52299
% households w low access to stores 25 y/o and older w bachelor's /1000	110.885	106.164	40.6371	122.654	118.332	43.6276
% White	80.8599	85.6959	15.0719	75.7593	79.6171	16.7522
% Black	11.3861	5.03010	14.6140	13.4737	7.90300	15.3919
% Asian	1.96190	1.22070	1.89220	3.67570	1.87900	5.28820
No of bars	29.3313	16.0000	39.0755	55.2143	23.5000	96.9646
No of grocery stores	42.5564	23.0000	67.0810	117.321	39.0000	16.5490
No of restaurants	13.1345	8.00000	13.1383	14.9219	9.00000	16.5490
% take public transportation	0.41130	0.19870	0.76870	1.24690	0.32130	6.14170

NOTES: Model *R* corresponds to Algorithm 1 where we use the sample correlation matrix. Group 1 and 2 are the obtained partitions \hat{G}_1 and \hat{G}_2 , respectively. Population Density is the number of people per sq mile; median household income is in the U.S. dollars; % Poverty is the poverty rate; % 1-person households is the percentage of one-person households; % 5 or more person households is the percentage of five or more person households; % households w 60 y/o and older is the percentage of households that have one or more members who are 60 years old or older; low access to stores is defined as living more than one mile (urban areas) or 10 miles (rural areas) from the nearest supermarket, supercenter, or large grocery store; /1000 is per 1000 persons; % take public transportation is the percentage of all persons who work in a county and take public transportation to work every day. All feature information is as of 2017.

t-tests on the fastest and slowest growth groups (Section 2.6) with respect to various demographic variables. The null and alternative hypotheses for this *t*-test for the *d*th feature are as follows:

$$H_0 : \mu_{d,1} = \mu_{d,2}, \text{ vs. } H_a : \mu_{d,1} \neq \mu_{d,2}, \tag{4}$$

where $\mu_{d,1}$ is the mean value of the *d*th feature of cluster 1 and $\mu_{d,2}$ is the mean value of the *d*th feature of cluster 2. We then compute the two-sample test statistic with pooled estimate of the variance. After finding the *p*-values, we rank the features from lowest *p*-value to highest.

Furthermore, we repeat Algorithm 1 for $K = 3, 4,$ and $5,$ select the “fastest” and “slowest” growth clusters in each case, and carry out the independent two-sample *t*-tests as described above for the same demographic features. This sensitivity analysis tests whether the demographic variables that are significantly different between the two groups are consistent when we have a larger number of communities. Ultimately, we present the statistically significant demographic features.

3.1. Data

For this section, we use data from Data Planet, a social science research database that compiles 12.6 billion U.S. and international datasets from over 80 sources. For our purposes, we look at the 2017 American Community Survey (ACS), the largest household survey in the United States, conducted by the U.S. Census Bureau. We select 17 relevant features on a county level, which are displayed and summarized in Table 4. Note that not all 950 counties from Johns Hopkins CCSE data that were used in Section 2.1 is available on Data Planet, thus the analysis is done on 633 counties for this section. Now, we are left with 301 counties in Group 1 and 332 counties in Group 2, which is still a close split like that of *R* seen in Table 2.

3.2. Results and Discussion

It is evident from Table 4 that community detection with *R* results in Group 2 (fast growth) containing counties with the highest mean and median population density by far (Figure 8 is a visualization of counties assigned to two categories based on density and median income). The mean and median household incomes are also higher for counties in Group 2. The mean number of persons 25 years old or older with bachelor's is noticeably greater for Group 2, which can often coincide with more urban areas that are more densely populated. However, it can also be related to the number of universities in a particular area, as a higher number would exacerbate the spread of COVID-19. The numbers of bars and grocery stores are also starkly different between the two groups. Moreover, the percentage of people who take public transportation to work is around three times greater for Group 2 than Group 1. On the other hand, unlike what one would expect in terms of the relationship between the number of one-person households and the spread of COVID-19, there is not much differentiation between the number of people in a household.

Table 5 contains the *p*-values for all of the 17 features. The numbers of grocery stores and the number of bars have much lower *p*-values (and are below the *p*-value threshold) than that of the number of restaurants. Also, as expected, the median household income is among the features with lower *p*-values, along with population density. After conducting the same two-sided *t*-tests for $K = 3, 4,$ and 5 on the two extreme groups (the groups that have the smallest and largest average growth rates further verified by plotting Figure 4 for $K = 3, 4,$ and 5 communities), the seven statistically significant features found are as follows: population density, median income, number of persons who are 25 years and older with bachelor's per 1000 persons, percentage of the White population, percentage of the Asian population, number of bars, and number of grocery stores. These seven features are consistently significant for each

Table 5. Left table is R clusters' p -values for independent two-sample t -tests for selected features between Group 1 and Group 2 sorted from the smallest to largest p -value.

Feature	P-Value	Feature	P-Value
% Asian	1.26E-11	No of grocery stores	2.85E-08
No of grocery stores	5.83E-11	% low income w low access to store	6.38E-07
No of bars	2.95E-06	Median household income	8.41E-06
% White	3.04E-06	% Poverty	2.01E-04
Median household income	1.44E-05	% White	0.01967
% households w low access to stores	1.60E-05	Population density	0.04027
25 y/o and older w Bachelor's /1000	2.80E-05	% 1-person households	0.07537
Population density	2.39E-04	% households w low access to stores	0.10640
% low income w low access to store	0.00303	% 5 or more persons households	0.10711
% take public transportation	0.00436	% Black	0.12222
% 5 or more persons households	0.02324	% take public transportation	0.13245
% Black	0.04672	% of households w 60 y/o and older	0.35344
% Poverty	0.10603	% Asian	0.47698
No of restaurants	0.11432	25 y/o and older w Bachelor's /1000	0.52498
% w low access to stores	0.13698	% w low access to stores	0.62138
% households w 60 y/o and older	0.18014	No of restaurants	0.89977
% 1-person households	0.63999	No of bars	0.90224

NOTE: Right table is recent data (05/10/2020–07/10/2020) R clusters' p -values. The features in bold are the ones that are selected as significant features for further analysis in Section 4.

$K = 2, 3, 4,$ and 5 based on p -values. These values form the demographic vector \mathbf{d}_i for each county i . The variables for bars and grocery stores underscore the ease of transmission in locations with greater numbers of public gathering spots, a characteristic evident in cities like New York City where most people choose to convene at bars without much social distancing (before stricter lockdowns took place).

After finding the growth communities and conducting t -tests to ascertain the significant features for the latter phase of the pandemic in the United States (05/10/2020–07/10/2020), the features with the lowest p -values diverge from those of earlier data, as presented in the right panel of Table 5. Population density and median income are still among the most meaningful but the percentage of people with low access to stores and the percentage living in poverty have become significant. This suggests that at later stages of the pandemic, poverty and other income-related measures become more indicative and responsible for the differences in case growth among counties. Thus, the seven features for \mathbf{d}_i for this latter phase are the top seven variables in Table 5: number of grocery stores, % low income with low access to stores, median household income, % poverty, % white, population density, and % 1-person households.

4. Prediction with Social Distancing Data

The final section of our COVID-19 methodology is to predict a county's growth trajectory a few days into the future. We propose a prediction methodology with the objective that given a new county, the new county's key demographic features, and social distancing measures, we implement an algorithm that projects the new county's future growth.

Before going in-depth on the prediction models, it's necessary to first define some important variables. Let l be the number of the days forward to be projected for a new county. To build such a predictive model, let $y_{i,t+l} = \log(x_{i,t+l}) - \log(x_{i,t})$ be county i 's l -day forward log-growth rate, which is close to the growth rate $\frac{x_{i,t+l} - x_{i,t}}{x_{i,t}}$ by Taylor's expansion and numerical verification, for $t = 1, \dots, T_i$. Here, $T_i + l$ is the total number of days where county i has 12 or more cases. Recall the obtained partitions from Algorithm 1 (set of indices

of counties that belong to group k): $\hat{G}_k = \{i \in [1, n] | \hat{Z}_i = k\}$, where $\hat{Z} \in \mathbb{R}^n$ is the recovered community label vector. For a community k , and a county $i \in \hat{G}_k$, let $\mathbf{d}_i \in \mathbb{R}^q$ be county i 's significant feature vectors obtained from Section 3, $\mathbf{S}_i = [s_1^i, s_2^i, \dots, s_{T_i}^i]^T \in \mathbb{R}^{T_i \times 3}$ be county i 's three social distancing time series matrix (see Section 4.1 for details about this data) and $\mathbf{y}_i = [y_{i,1+l}, \dots, y_{i,T_i+l}]^T \in \mathbb{R}^{T_i}$ be its l -day forward log case difference. Note that each row of \mathbf{S}_i , $\mathbf{s}_t^i \in \mathbb{R}^3$, has three different social distancing metrics at time t .

In summary, we have data $\{\mathbf{S}_i, \mathbf{y}_i : i \in \hat{G}_k\}$ for training an l -day ahead predictive model for the k^{th} community. Also, to recover the predicted log cases $\log(\hat{x}_{i,t+l})$ for county i on day $t + l$, one can simply use $\log(\hat{x}_{i,t+l}) = \hat{y}_{i,t+l} + \log(x_{i,t})$.

4.1. Data

Social distancing data is courtesy of Unacast and its COVID-19 Social Distancing Scoreboard. The scoreboard tracks mobile device movement and has three metrics that quantify the level of social distancing people in a particular county are practicing. The first metric is the percentage change in total distance traveled, averaged across all devices, compared to a pre-Corona baseline. The second is the percentage change in the number of visitations to nonessential places, compared to a pre-Corona baseline. For these two metrics, the pre-Corona baseline of a county on a particular day is defined as the average of the four corresponding pre-weekdays (at least four weeks before the day). For example, for Monday 3/30, the pre-Corona baseline of the first metric is the average of the first metric for the four Mondays: 2/10, 2/17, 2/24, and 3/2. The final metric is the rate of human encounters as a fraction of the pre-Corona national baseline. The pre-Corona national baseline for this metric is the average of the metric taken over four weeks that immediately precede the COVID-19 outbreak (02/10/2020 - 03/08/2020) as defined by Unacast. Since this data starts at 02/25/2020 which is after the start of the Coronavirus cases data (01/22/2020), we perform prediction on the period 02/25/2020 - 7/10/2020, which is the start of the "initial phase" until the end of the "recent phase." Also note that not all counties from Johns Hopkins CCSE data and Data Planet are available at Unacast's database so out

of the 633 counties from Section 3.1, this section is performed on 627 counties.

4.2. Long Short-Term Memory Network

To enhance the effectiveness of the model, we take advantage of a special type of recurrent neural network (RNN): long short-term memory (LSTM) networks, which are designed for time-series forecasting. Unlike feedforward neural networks (FNNs), RNNs produce an output that depends on a “hidden” state vector that contains information based on prior inputs and outputs. LSTMs builds on a simple, vanilla RNN to include a forget gate, input gate, and output gate for each module. Hence, it is able to “remember” information for longer time periods (lags). The output for an LSTM module at time t is as follows:

$$h_t = o_t \tanh(C_t), \quad \tanh(x) = \frac{\exp(x) - \exp(-x)}{\exp(x) + \exp(-x)}. \quad (5)$$

The components of h_t are broken down as follows: $f_t = \sigma(W_f[h_{t-1}, x_t] + b_f)$, is the forget gate output and W_f and b_f are its weights and biases, respectively. $i_t = \sigma(W_i[h_{t-1}, x_t] + b_i)$, is its input gate output and W_i and b_i are its weights and biases, respectively. The cell state vector then gets updated by forgetting the previous memory through the forget gate and adding new memory through the input gate: $C_t = f_t C_{t-1} + i_t \tilde{C}_t$, where $\tilde{C}_t = \tanh(W_C[h_{t-1}, x_t] + b_C)$. Subsequently, the output gate $o_t = \sigma(W_o[h_{t-1}, x_t] + b_o)$ and W_o and b_o are its weights and biases, respectively. Here, $\sigma(x) = (1 + \exp(-x))^{-1}$ is the sigmoid activation function.

We also compare the LSTM’s performance with that of an FNN, namely an MLP (multilayer perceptron). MLPs are a type of fully connected FNN first introduced and popularized by Rumelhart, Hinton, and Williams (1986), consisting of an input layer, output layer, and hidden layers in between, where the training process is done through backpropagation. The total input x_i^{s+1} of a neuron i of layer $s + 1$ takes the form of

$$x_i^{s+1} = \sum_j h_{ij}^s x_{\sigma_j}^s + b_i^{s+1}, \quad (6)$$

where h_{ij}^s is the weight for neuron j of the previous layer s to neuron i of layer $s + 1$ and b_i^{s+1} is the bias of layer $s + 1$. $x_{\sigma_j}^s = \sigma(x_j^s)$ is the output from neuron j from the previous layer s , where a nonlinear activation function $\sigma(\cdot)$ is applied to the input. Most common activation functions include sigmoid, tanh, or ReLU (rectified linear unit), where the ReLU often learns faster in deeper networks.

4.3. Prediction Models

The first prediction model, Algorithm 2 (which we will refer to as SD-LSTM, where Sd stands for social distancing), is a prediction procedure that solely uses a nonlinear model (a neural network) to fit the data. The idea is to first train an LSTM for each of the K communities, and then given a new county, we select the corresponding fitted model for prediction from our repertoire with respect to its nearest neighbor county (in demographic variables, not geographical distance). That is, we apply the nearest neighborhood to the demographic variables

to classify the new county’s community, and use the model for that community to forecast the county’s cases. Specifically, for each community $k \in \{1, \dots, K\}$, we train an LSTM with the data $\{(s_t^i, y_{i,t+l})_{t=1}^{T_i}, \forall i \in \hat{G}_k\}$ and this depends on the numbers of steps forward, l , we are trying to forecast. For simplicity of notation, for community k , we denote all such data items for all counties $i \in \hat{G}_k$ by $\{(s_t, y_{t+l}), t \in \hat{G}_k^l\}$ and the fitted function by $\hat{f}_k^l(\cdot)$. Now the second part, the prediction, is that given a new county i ’s demographic data $\mathbf{d}_{i'}$ and social distancing information $\mathbf{S}_{i'} = [s_1^i, s_2^i, \dots, s_{T_{i'}}^i] \in \mathbb{R}^{T_{i'} \times 3}$, we first find its nearest neighbor county $j = \operatorname{argmin}_j \|\mathbf{d}_{i'} - \mathbf{d}_j\|^2$ and its associated community \hat{Z}_j and use its associated prediction model to predict $\hat{y}_{i',t+l} = \hat{f}_{k'}^l(s_t^i), t = 1, \dots, T_{i'}$ with $k' = \hat{Z}_j$. Algorithm 2 summarizes this method of prediction.

To predict a future event, the above procedure gives a number of prediction methods. For example, to predict tomorrow’s outcome, we can use today’s social distancing data with $l = 1$, or yesterday’s social distancing data with $l = 2$, or the day before yesterday’s social distancing data with $l = 3$, and so on. As verified later in Figure 10, it turns out that $l = 4$ is the best choice of lead, which approximately aligns with the incubation period of the disease.

Algorithm 2 SD-LSTM: LSTM Prediction

Part I: Training

Input: The lead l

- 1: **for** $k \in \{1, \dots, K\}$ **do**
- 2: Train LSTM $\hat{f}_k^l(\cdot)$ using the data $\{(s_t, y_{t+l}), t \in \hat{G}_k^l\}$.
- 3: **end for**
- 4: **return** fitted LSTMs $\hat{f}_k^l(\cdot), k = 1, \dots, K$.

Part II: Prediction

Input: A new county i' , $\mathbf{d}_{i'} \in \mathbb{R}^q$, $\mathbf{S}_{i'} = [s_1^i, s_2^i, \dots, s_{T_{i'}}^i] \in \mathbb{R}^{T_{i'} \times 3}$, \hat{Z} and $\hat{f}_k^l(\cdot), k = 1, \dots, K$ from Part I.

- 1: Find county i ’s nearest neighbor $j = \operatorname{argmin}_j \|\mathbf{d}_{i'} - \mathbf{d}_j\|^2$.
 - 2: Select $\hat{f}_{k'}^l(\cdot)$, where $k' = \hat{Z}_j$.
 - 3: **for** $t \in \{1, \dots, T_{i'}\}$ **do**
 - 4: $\hat{y}_{i',t+l} = \hat{f}_{k'}^l(s_t^i)$.
 - 5: **end for**
 - 6: **return** $\hat{\mathbf{y}}_{i'} = [\hat{y}_{i',1+l}, \hat{y}_{i',2+l}, \dots, \hat{y}_{i',T_{i'}+l}]^T \in \mathbb{R}^{T_{i'}}$.
-

Algorithm 3 takes SD-LSTM a step further to include a linear component, namely, fitting the linear model for each county first with residuals from each community then further modeling with an LSTM. This idea is related to boosting or nonparametric estimation using a parametric start (Fan, Wu, and Feng 2009), resulting in a semiparametric fit. Again, the objective of the training part is to obtain K fitted models, one for each community, using semiparametric regression techniques. More specifically, for county i with lead l , we first fit the following linear regression models

$$y_{i,t+l} = \alpha_i^l + (s_t^i)^T \beta_i^l + \varepsilon_{i,t+l}, \quad t = 1, \dots, T_i. \quad (7)$$

After fitting the linear regression models for every county $i \in \hat{G}_k^l$, we obtain the residuals $\{\hat{\varepsilon}_{i,t+l}, t \in \hat{G}_k^l\}$ and save all the coefficients α_i^l, β_i^l for $i \in \hat{G}_k^l, k = 1, \dots, K$. We then extract

the information further from $\{(s_t, \hat{e}_{t+l}), t \in \hat{G}_k^l\}$ by fitting an LSTM to obtain the fitted $\hat{g}_k^l(\cdot)$. Then, for the prediction of the new county i' , we follow the same steps as those in SD-LSTM but the final prediction is instead adding the linear fit of the nearest neighbor county and the LSTM fit of the community corresponding to the nearest neighbor county:

$$\hat{y}_{i',t+l} = \alpha_j^l + (s_t^{i'})^T \beta_j^l + \hat{g}_k^l(s_t^{i'}),$$

where $k' = \hat{Z}_j$. We will refer to this model as SD-SP. The idea is summarized in [Algorithm 3](#).

Algorithm 3 SD-SP: Semi-parametric Prediction

Part I: Training

Input: The lead l

- 1: **for** $k \in \{1, \dots, K\}$ **do**
- 2: Fit the regression models (7) for $i \in \hat{G}_k^l$ and obtain the residuals $\{\hat{e}_{t+l}, t \in \hat{G}_k^l\}$.
- 3: Train LSTM using $\{(s_t, \hat{e}_{t+l}), t \in \hat{G}_k^l\}$
- 4: **end for**
- 5: **return** fitted LSTMs $\hat{g}_k^l(\cdot)$ and all α_i^l and β_i^l for $i \in \hat{G}_k^l, k = 1, \dots, K$.

Part II: Prediction

Input A new county i' , $\mathbf{d}_{i'} \in \mathbb{R}^q$, $\mathbf{S}_{i'} = [s_1^{i'}, s_2^{i'}, \dots, s_{T_{i'}}^{i'}] \in \mathbb{R}^{T_{i'} \times 3}$, $\hat{\mathbf{Z}}$ and $\hat{g}_k^l(\cdot)$, α_i^l and β_i^l for $i \in \hat{G}_k^l, k = 1, \dots, K$ from Part I.

- 1: Find county i' 's nearest neighbor $j = \operatorname{argmin}_j \|\mathbf{d}_{i'} - \mathbf{d}_j\|^2$.
 - 2: Select α_j^l and β_j^l for county j .
 - 3: Select $\hat{g}_k^l(\cdot)$, where $k' = \hat{Z}_j$.
 - 4: **for** $t \in \{1, \dots, T_{i'}\}$ **do**
 - 5: $\hat{y}_{i',t+l} = \alpha_j^l + (s_t^{i'})^T \beta_j^l + \hat{g}_k^l(s_t^{i'})$.
 - 6: **end for**
 - 7: **return** $\hat{\mathbf{y}}_{i'} = [\hat{y}_{i',1+l}, \hat{y}_{i',2+l}, \dots, \hat{y}_{i',T_i+l}]^T \in \mathbb{R}^{T_{i'}}$.
-

We also include three other algorithms for comparison purposes. The first replaces the LSTM fit $\hat{f}_k^l(\cdot)$ of community k in SD-LSTM with a linear model. This corresponds to fitting (7) without further boosting by an LSTM. For simplicity, we shall refer to this approach as the SD-LM (social distancing linear model). The second one is to use both demographic and social distancing data to fit an LSTM. This approach is identical to SD-LSTM, but includes the $q = 7$ significant demographic variables in [Table 5](#) in addition to the three social distancing variables. Similarly, we shall refer to this approach as the DSD-LSTM (demographic and social distancing LSTM). DSD-LSTM is expected to improve the performance of [Algorithm 2](#) due to the additional information from the demographic variables. The final model is similar to SD-LSTM but instead of an LSTM, we use an MLP with two hidden layers (we will refer to this model as SD-MLP).

4.4. Implementation

For the LSTM, the optimization algorithm used is Adam with a learning rate of 0.01. For regularization purposes, we also use a dropout layer (dropout rate of 0.5) for each of the LSTMs. This

also helps take care of any potential multi-collinearity between the demographic features that are used in Model 4. We also test the performance of various lags to see which yields the highest out-of-sample R^2 , defined as follows for a given new county i' and lead l :

$$1 - \frac{\sum_{t=1}^{T_{i'}} (y_{i',t+l} - \hat{y}_{i',t+l})^2}{\sum_{t=1}^{T_{i'}} (y_{i',t+l} - \bar{y}_{i',t+l})^2}, \quad (8)$$

where $y_{i',t+l}$ is the observed value, $\hat{y}_{i',t+l}$ is the predicted value, and $\bar{y}_{i',t+l} = 1/T_{i'} \sum_{t=1}^{T_{i'}} y_{i',t+l}$, serving as the baseline predictor. The average, median, and standard deviation of the R^2 values are then taken across all counties in the testing sample. Additionally, for any model involving an LSTM, up to the minimum length $\tilde{T} = \min_{i=1, \dots, n} T_i$ is taken for each county since the LSTM needs

each sample to have uniform time steps. Therefore, $T_i = \tilde{T}$ for each county i in the case of SD-LSTM, SD-SP, and the DSD-LSTM model. For information regarding the hidden layers used and input shapes in the neural network models, see [Table 6](#).

Due to the nature of neural networks and considering the relatively small sample size, we conduct five-fold cross-validation to evaluate the learning models. We divide all the counties into five train-test splits, where the correlation matrix is re-calculated on only the training set. Then, for each $K = 1, \dots, 5$, [Algorithm 1](#) is executed on the training set for that particular split. Hence, we have 25 sets of results for each model (five for each of the five train-test splits).

4.5. Results and Discussion

Among the four prediction models we implemented using the county-level social distancing measures (see [Section 4.1](#)), for $K = 1, 2, 3$, Model 4 (DSD-LSTM) slightly outperforms Model 1 due to the use of the seven additional demographic variables. Model 1 (SD-LSTM) proves to result in the highest average and median out-of-sample R^2 for $K = 4, 5$. Models 2 (SD-SP) and 3 (SD-LM) have much poorer performance across the board, which implies that these two models are worse than a horizontal line fit. It is also worth mentioning that the neural network correction part of Model 2 is incredibly hard to tune to be able to outperform the linear model Model 3 on its own. In this case, not only was it not able to enhance Model 3's results, Model 2's correction actually worsened the model's predictive ability. Other nonparametric methods other than a neural network were also used (such as support vector regression) but all had a similar lackluster effect, implying that boosting or enhancing the linear estimator with a nonlinear estimator is not beneficial in this case. Model 1's and Model 4's superiority suggests a

Table 6. Number of hidden layers, the type and number of nodes of each hidden layer, and input shape of each model that contains an NN.

	No. of hidden layers	Type and no of nodes/dropout rate	Input shape
SD-LSTM	1	LSTM 10, Dropout (0.5)	$n \times \tilde{T} \times 3$
SD-SP	1	LSTM 10, Dropout (0.5)	$n \times \tilde{T} \times 3$
DSD-LSTM	1	LSTM 10, Dropout (0.5)	$n \times \tilde{T} \times 10$
SD-MLP	2	Dense 10, Dropout (0.5), Dense 10, Dropout (0.5)	$\sum_{i=1}^n T_i \times 3$

Table 7. 02/25/2020–7/10/2020 in-sample and out-of-sample R^2 for Model 1 (SD-LSTM), Model 2 (SD-SP), Model 3 (SD-LM), Model 4 (DSD-LSTM), and Model 5 (SD-MLP) for $K = 1, 2, 3, 4$, and 5.

Model	In-Sample			Out-of-Sample		
	Mean	Median	Std Dev	Mean	Median	Std Dev
Model 1, $K = 1$	0.3447	0.6376	0.8642	0.3281	0.6192	0.7978
Model 1, $K = 1^*$	0.3532	0.6224	0.8050	0.1841	0.5346	1.6523
Model 1, $K = 2$	0.4733	0.6372	0.5632	0.2170	0.5437	1.0514
Model 1, $K = 3$	0.5003	0.6527	0.5186	0.2792	0.5600	0.8986
Model 1, $K = 4$	0.5211	0.6580	0.4738	0.2485	0.5245	0.9007
Model 1, $K = 5$	0.5113	0.6593	0.5094	0.2024	0.5461	1.0277
Model 2, $K = 1$	-2.0229	-1.8148	0.9800	-2.9663	-1.9824	7.8948
Model 2, $K = 2$	-1.8886	-1.7337	0.8901	-2.9613	-1.8356	8.1548
Model 2, $K = 3$	-1.8819	-1.6990	0.8471	-2.9393	-1.7641	8.0641
Model 2, $K = 4$	-1.8647	-1.7513	0.8371	-2.9220	-1.7512	8.1715
Model 2, $K = 5$	-1.8673	-1.7500	0.8016	-2.9281	-1.7872	8.0991
Model 3, $K = 1$	-0.1227	-0.0271	0.3236	-0.1458	-0.0311	0.4000
Model 3, $K = 2$	-0.1148	-0.0260	0.2941	-0.1586	-0.0296	0.5145
Model 3, $K = 3$	-0.1138	-0.0252	0.2936	-0.1563	-0.0276	0.5054
Model 3, $K = 4$	-0.1095	-0.0239	0.2771	-0.1659	-0.0302	0.6044
Model 3, $K = 5$	-0.0991	-0.0246	0.2559	-0.1542	-0.0317	0.5320
Model 4, $K = 1$	0.4855	0.6429	0.5114	0.4513	0.6251	0.5384
Model 4, $K = 2$	0.5486	0.6645	0.3786	0.3567	0.5556	0.7031
Model 4, $K = 3$	0.5473	0.6554	0.3952	0.3611	0.5672	0.6536
Model 4, $K = 4$	0.5489	0.6522	0.3930	0.2947	0.4912	0.7717
Model 4, $K = 5$	0.5467	0.6550	0.3812	0.2516	0.5223	0.8706
Model 5, $K = 1$	-0.1894	-0.0394	0.4866	-0.2098	-0.0430	0.4551
Model 5, $K = 2$	-0.1507	-0.0365	0.3679	-0.1886	-0.0411	0.4241
Model 5, $K = 3$	-0.1432	-0.0383	0.3538	-0.1729	-0.0415	0.3932
Model 5, $K = 4$	-0.1318	-0.0415	0.3072	-0.1362	-0.0413	0.3277
Model 5, $K = 5$	-0.1206	-0.0374	0.2633	-0.1560	-0.0462	0.3741

NOTES: *Same as Model 1, $K = 1$ but only uses half of the counties ($n = 250$), which are randomly sampled. The average values for mean, median and standard deviation are taken for each of the 5 folds. For $K = 1$, we assume that all counties belong to one group so we take all counties in the training data to train the neural network. The results are based on $l = 4$ and a five-fold cross-validation. 501 of the total 627 counties are used as training data (in-sample) and 126 counties are used as testing data (out-of-sample).

nonlinear effect that the LSTM was able to extract, but the linear, semi-parametric, and MLP were unable to do so.

For Models 1 and 4, stratifying the communities through our method does make a difference in-sample since increasing K improves the models' mean and median in-sample R^2 . However, this is not the case for out-of-sample as $K = 1$ produces the best results (no heterogeneity) and the out-of-sample R^2 continues to drop from $K = 2$ to 5. It is reasonable to conclude that the decrease in sample size for each community training (e.g., $K = 1$ uses all 501 counties to train while $K = 5$ uses on average 1/5th of that number to train each community) is hurting the model's ability to take advantage of the heterogeneity embedded in the communities. Thus, since neural networks have an advantage in large sample size settings, the effect of the reduction in sample size for larger K s outweighs the community difference captured by community detection (Algorithm 1). We also include Model 5 (an FNN with two hidden layers, each with 50% dropout) to contrast the LSTM with. The performance is similar to Model 3 in that it is no better than a constant fit. The advantage of the LSTM is highlighted here since the output is dependent on previous computations, unlike the FNN that assumes the inputs (as well as outputs) are independent of each other. As COVID-19 cases are sequential information, the LSTM is clearly preferable to predict with. See Table 7 for the detailed breakdown by model and by the number of clusters K . Figure 9 contains the out-of-sample R^2 box plots for the four models with $K = 1, 2, 3, 4, 5$.

To ascertain whether using information from community detection still plays a role despite $K = 1$ being the best setting for out-of-sample prediction, we carry out two further tests. The first test is random sampling half (250) of the counties used for $K = 1$ ($n = 501$), which roughly downsamples to the sample size used to fit a model for each community for $K = 2$. This achieves the effect of equaling the sample sizes between $K = 1$ and $K = 2$ for a fair comparison of their performance. We test this only with Model 1 and depict the results in the "Model 1, $K = 1^*$ " row in Table 7. They show that after removing the effect of sample size, having two communities produces a better predictive outcome. In particular, the out-of-sample mean and median R^2 0.1841 and 0.5346 are lower than 0.2170 and 0.5437 for $K = 2$. We also see that the standard deviation for one community is much higher than that of using two communities. The second test involves randomly assigning each training county to a community instead of using our community detection procedure from Section 2. As shown in Table 8, after repeating this five times for Model 1, $K = 2$, the median in-sample R^2 values are much lower compared to that of the same model in Table 7 (median of 0.5569 vs. 0.6372, respectively). Albeit a smaller difference, the out-of-sample median 0.4980 is also smaller than the 0.5437 in Table 7. Together, these two results demonstrate that community detection and separation aid in predictive performance and categorization of the nature of the counties' growth trajectories; however, this effect is likely masked by the diminishing sample size as K increases.

Also note that before obtaining the prediction results for each algorithm, the hyperparameter of the appropriate lead was chosen by comparing the average R^2 values for each lead. The left panel of Figure 10 presents the median out-of-sample R^2 vs. $l = 1, \dots, 7$ for the two best models Model 1, $K = 1$, and Model 4, $K = 1$ as examples. Since out-of-sample R^2 plateaus after a four-day lead, we fixed $l = 4$ as a larger lead would decrease precision and it is important to be consistent with studies that show the median incubation period of COVID-19 is 4 and 5 days (Guan et al. 2020; Lauer et al. 2020). Furthermore, anything longer than a week or so is rarely used in epidemiological and sociological studies.

In addition, we establish the importance and impact of using social distancing features for prediction in this section via two methodologies. First of all, instead of the social distancing scores as input S_i , we replace them with unvarying constants (to purposely not fully use the information of social distancing data). Table 9 features the results for Model 1 carried out with constant social distancing scores. Compared to each corresponding number of communities in Table 7, the out-of-sample mean and median are all significantly lower, which indicates that social distancing behavior has clear forecasting power. Without full signal from the social distancing input, predictive capabilities are incontrovertibly reduced. Afterward, to discover the relative effect of each of the three social distancing scores, we average out-of-sample R^2 after leaving each feature out one at a time. Evidently, the right panel of Figure 10 suggests that although there is no distinct drop in performance, leaving out feature 1 (percent change in total distance traveled) results in the largest decline in R^2 whereas leaving out feature 2 (percent change in the number of visitations to non-essential places) results in the smallest decline.

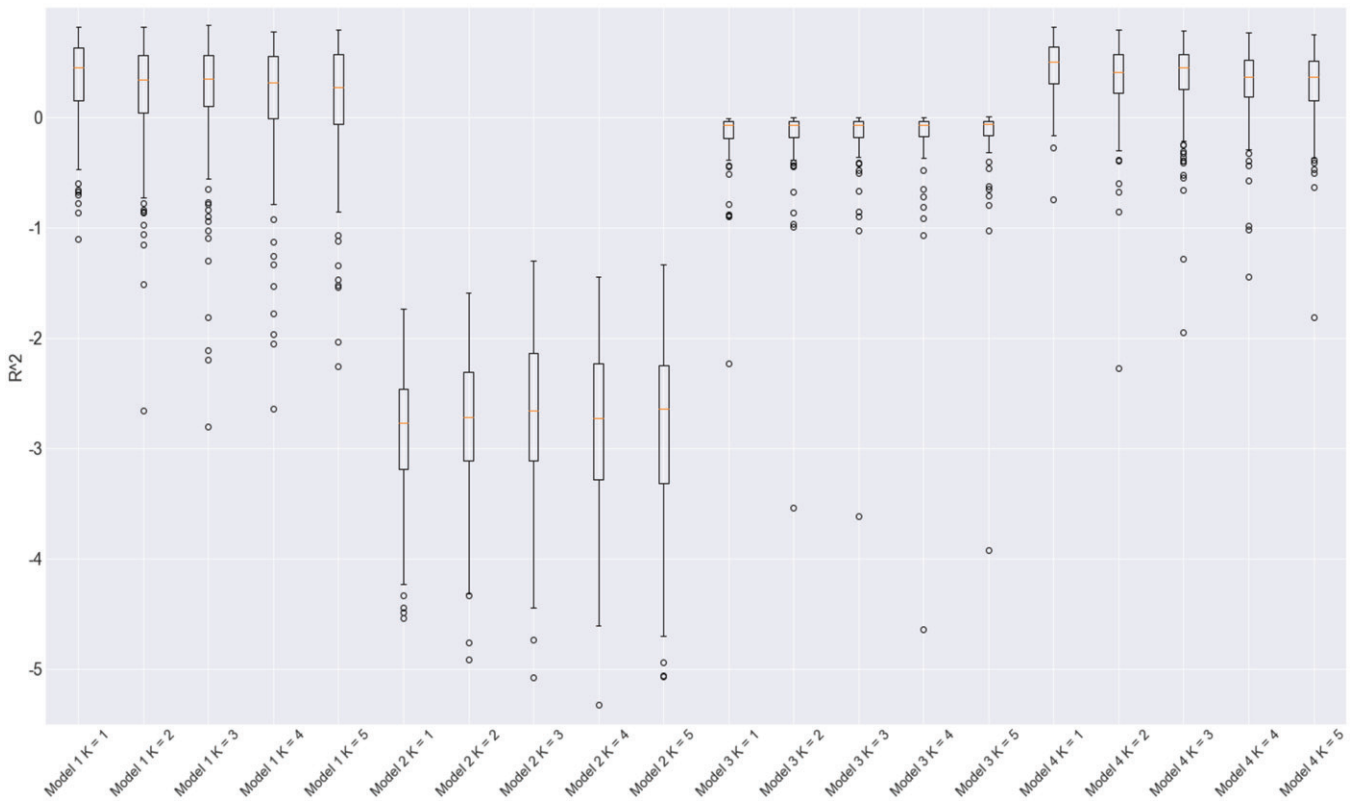


Figure 9. Out-of-sample R^2 boxplots for all counties using Model 1 (SD-LSTM), Model 2 (SD-SP), Model 3 (SD-LM), and Model 4 (DSD-LSTM) for $K = 1, 2, 3, 4, 5$. The results are based on $l = 4$ and the period 02/25/2020 - 7/10/2020.

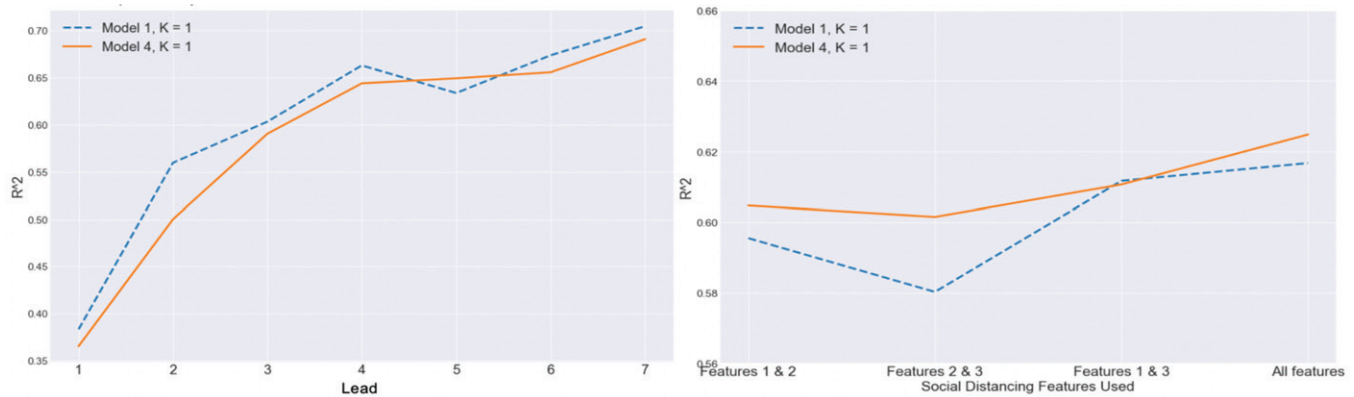


Figure 10. The left panel is the average out-of-sample R^2 for Model 1, $K = 1$ and Model 4, $K = 1$ for $l = 1, 2, 3, 4, 5, 6, 7$ for one train-test split. The right panel is average out-of-sample R^2 for the same models, where one social distancing feature is left out each time. Both panels are of the phase 02/25/2020–7/10/2020 and based on five-fold cross-validation.

Table 8. 02/25/2020–7/10/2020 random assignment in-sample and out-of-sample R^2 for Model 1 (SD-LSTM), $K = 2$.

	In-Sample			Out-of-Sample		
	Mean	Median	Std Dev	Mean	Median	Std Dev
Trial 1	0.2349	0.4842	0.9238	0.4523	0.4956	0.3505
Trial 2	0.2764	0.5569	0.9678	0.3304	0.4995	0.7916
Trial 3	0.2921	0.5628	0.9442	0.1163	0.4980	1.4862
Trial 4	0.2900	0.5594	0.9677	0.3410	0.5454	0.7049
Trial 5	0.3404	0.5430	0.8943	-0.0455	0.4367	1.3895
Median	0.2900	0.5569	0.9442	0.3304	0.4980	0.7916

NOTE: Each trial is completed via randomly assigning each train county of one of the train-test splits to either community 1 or community 2.

Table 9. 02/25/2020–7/10/2020 in-sample and out-of-sample R^2 for Model 1 (SD-LSTM) but with constant social distancing scores.

	In-Sample			Out-of-Sample		
	Mean	Median	Std Dev	Mean	Median	Std Dev
Model 1, $K = 1$	0.2595	0.5045	0.9772	0.1966	0.4596	1.2634
Model 1, $K = 2$	0.3061	0.5399	0.9073	0.0705	0.4023	1.4220
Model 1, $K = 3$	0.3244	0.5327	0.8876	0.1303	0.4088	1.1456
Model 1, $K = 4$	0.3366	0.5423	0.8621	0.1175	0.4197	1.2352
Model 1, $K = 5$	0.3238	0.5353	0.8662	0.0760	0.3919	1.3346

5. Conclusion

By using spectral clustering, we develop a framework to detect COVID-19 communities and discover meaningful interpretations of the clusters. We use the correlation matrix instead of the canonical Laplacian as it offers more meaningful insights and more distinct clusters. The resulting communities are distinct in the nature of their respective growth trajectories and there are several demographic variables that further distinguish these growth communities. Singling out the significant demographic features that have explanatory power of a county's growth community membership, we discover that not all of these variables are intuitive when it comes to their role in impacting COVID-19 cases.

After modeling and interpreting historical disease progression, we turn to study future growth trajectories by incorporating social distancing information. We are able to reliably predict the logarithmic trends in case growth through the use of LSTMs and also verify that the counties are far from homogeneous—the obtained communities contain crucial information necessary for in-sample prediction. As for the LSTM's out-of-sample predictive power, the effect of the decline in sample size when increasing the stratification of counties into more communities dominates the heterogeneity between the counties' growth curves that community detection uncovers. However, after comparing results to randomly assigning counties to different communities, the method we propose still demonstrates that using the community detection results boosts the models' predictive performance.

We do, therefore, acknowledge that there could be other latent features that we did not capture in this study and that the three social distancing metrics used here may not paint the complete picture. Furthermore, we do not address the effect of government intervention at given time points that may have altered the disease progression. These could all be points that can be further investigated. Despite these potential shortcomings, the analysis conducted on the first phase of the disease here can also be compared to the second phase, which we are currently experiencing. As the United States and many other countries are witnessing an even more extraordinary uptick in cases again, we foresee several possible future applications of our study, including to other contagious disease outbreaks. Another interesting future work is to use the confidence distribution framework (Xie, Singh, and Strawderman 2011) to combine studies from independent data sources from different countries.

Supplementary Material

Supplementary material provides the algorithm and results when clustering using the regular adjacency matrices as described in Section 2.2.

Acknowledgments

We are grateful to the editor, the AE, and anonymous reviewers for their insightful comments which have greatly improved the scope and quality of the paper. We would like to thank Unicast Inc. for providing us with their extensive social distancing data.

Funding

Tang was supported by NSF Grant DMS-1712591. Feng was supported by NSF Grants DMS-2013789 and DMS-2034022. Fan was supported by NIH funding: Grant 5R01-GM072611-16.

References

- Abbe, E. (2017), "Community Detection and Stochastic Block Models: Recent Developments," *The Journal of Machine Learning Research*, 18, 6446–6531. [493,494]
- Abbe, E., Fan, J., Wang, K., and Zhong, Y. (2020), "Entrywise Eigenvector Analysis of Random Matrices With Low Expected Rank," *Annals of Statistics*, 48, 1452–1474. [494,495]
- Balakrishnan, S., Xu, M., Krishnamurthy, A., and Singh, A. (2011), "Noise Thresholds for Spectral Clustering," *Advances in Neural Information Processing Systems*, 24, 954–962. [493]
- Betensky, R. A., and Feng, Y. (2020), "Accounting for Incomplete Testing in the Estimation of Epidemic Parameters," *International Journal of Epidemiology*, 49, 1419–1426. [492]
- Brownlees, C., Gudmundsson, G. S., and Lugosi, G. (2020+), "Community Detection in Partial Correlation Network Models," *Journal of Business & Economic Statistics*, 1–11 (to appear). [493]
- Chen, J., and Yuan, B. (2006), "Detecting Functional Modules in the Yeast Protein-Protein Interaction Network," *Bioinformatics*, 22, 2283–2290. [492]
- Chen, Y., Chi, Y., Fan, J., and Ma, C. (2020), "Spectral Methods for Data Science: A Statistical Perspective," arXiv preprint arXiv:2012.08496. [493,494]
- Dowd, J. B., Andriano, L., Brazel, D. M., Rotondi, V., Block, P., Ding, X., Liu, Y., and Mills, M. C. (2020), "Demographic Science Aids in Understanding the Spread and Fatality Rates of Covid-19," *Proceedings of the National Academy of Sciences*, 117, 9696–9698. [493]
- Fan, J., Guo, J., and Zheng, S. (2020), "Estimating Number of Factors by Adjusted Eigenvalues Thresholding," *Journal of the American Statistical Association*, 1–33 (to appear). [495]
- Fan, J., Wu, Y., and Feng, Y. (2009), "Local Quasi-likelihood With a Parametric Guide," *Annals of Statistics*, 37, 4153–4183. [501]
- Fanelli, D., and Piazza, F. (2020), "Analysis and Forecast of Covid-19 Spreading in China, Italy and France," *Chaos, Solitons & Fractals*, 134, 109761. [493]
- Gilbert, M., Pullano, G., Pinotti, F., Valdano, E., Poletto, C., Boëlle, P.-Y., D'Ortenzio, E., Yazdanpanah, Y., Eholie, S. P., Altmann, M., Gutierrez, B., Kraemer, M. U. G., and Colizza, V. (2020), "Preparedness and Vulnerability of African Countries Against Importations of Covid-19: A Modelling Study," *Lancet*, 395, 871–877. [493]
- Guan, W.-j., Ni, Z.-y., Hu, Y., Liang, W.-h., Ou, C.-q., He, J.-x., Liu, L., Shan, H., Lei, C.-l., Hui, D. S., Du, B., Li, L.-j., Zeng, G., Yuen, K.-Y., Chen, R.-c., Tang, C.-l., Wang, T., Chen, P.-y., Xiang, J., Li, S.-y., Wang, J.-l., Liang, Z.-j., Peng, Y.-x., Wei, L., Liu, Y., Hu, Y.-h., Peng, P., Wang, J.-m., Liu, J.-y., Chen, Z., Li, G., Zheng, Z.-j., Qiu, S.-q., Luo, J., Ye, C.-j., Zhu, S.-y., and Zhong, N.-s. (2020), "Clinical Characteristics of Coronavirus Disease 2019 in China," *New England Journal of Medicine*, 382, 1708–1720. [503]
- Holland, P. W., Laskey, K. B., and Leinhardt, S. (1983), "Stochastic Block-models: First Steps," *Social Networks*, 5, 109 – 137. [492]
- Hong, H. G., and Li, Y. (2020), "Estimation of Time-varying Reproduction Numbers Underlying Epidemiological Processes: A New Statistical Tool for the Covid-19 Pandemic," *PloS One*, 15, e0236464. [492]
- Hu, Z., Ge, Q., Jin, L., and Xiong, M. (2020), "Artificial Intelligence Forecasting of Covid-19 in China," arXiv:2002.07112. [493]
- Im, H., Ahn, C., Wang, P., and Chen, C. (2020), "An Early Examination: Psychological, Health, and Economic Correlates and Determinants of Social Distancing Amidst Covid-19," PsyArXiv, doi:10.31234/osf.io/9ravu. [493]
- Jin, J. (2015), "Fast Community Detection by Score," *Annals of Statistics*, 43, 57–89. [493,495]
- Kucharski, A., Russell, T., Diamond, C., Liu, Y., Edmunds, J., Funk, S., Eggo, R., Sun, F., Jit, M., Munday, J., Davies, N., Gimma, A., Zandvoort, K., Gibbs, H., Hellewell, J., Jarvis, C., Clifford, S., Quilty, B., Bosse, N., and Flasche, S. (2020), "Early Dynamics of Transmission and Control

- of Covid-19: A Mathematical Modelling Study,” *The Lancet Infectious Diseases*, 20, 553–558. [492]
- Lauer, S. A., Grantz, K. H., Bi, Q., Jones, F. K., Zheng, Q., Meredith, H., Azman, A. S., Reich, N. G., and Lessler, J. (2020), “The Incubation Period of 2019-nCoV from Publicly Reported Confirmed Cases: Estimation and Application,” *Annals of Internal Medicine*, 172, 577–582. [503]
- Lei, J. and Rinaldo, A. (2015), “Consistency of Spectral Clustering in Stochastic Block Models,” *Annals of Statistics*, 43, 215–237. [493,495]
- Lippi, G., Mattiuzzi, C., Sanchis-Gomar, F., and Henry, B. M. (2020), “Clinical and Demographic Characteristics of Patients Dying From Covid-19 in Italy vs. China,” *Journal of Medical Virology*, 92, 1759–1760. [493]
- Liu, Z., magal, p., Seydi, O., and Webb, G. (2020), “Predicting the Cumulative Number of Cases for the Covid-19 Epidemic in China From Early Data,” *Mathematical Biosciences and Engineering*, 17, 3040–3051. [493]
- Ng, A. Y., Jordan, M. I., and Weiss, Y. (2001), “On Spectral Clustering: Analysis and an Algorithm,” in *Advances in Neural Information Processing Systems*, T. Dietterich and S. Becker and Z. Ghahramani, eds., 849–856. Vancouver, BC: MIT Press. [493]
- Peng, L., Yang, W., Zhang, D., Zhuge, C., and Hong, L. (2020), “Epidemic Analysis of Covid-19 in China by Dynamical Modeling,” medRxiv. [492]
- Rajapakse, J. C., Gupta, S., and Sui, X. (2017), “Fitting Networks Models for Functional Brain Connectivity,” in *2017 IEEE 14th International Symposium on Biomedical Imaging (ISBI 2017)*, 515–519. [492]
- Roda, W. C., Varughese, M. B., Han, D., and Li, M. Y. (2020), “Why is It Difficult to Accurately Predict the Covid-19 Epidemic?” *Infectious Disease Modelling*, 5, 271 – 281. [493]
- Rohe, K., Chatterjee, S., and Yu, B. (2011), “Spectral Clustering and the High-dimensional Stochastic Blockmodel,” *The Annals of Statistics*, 39, 1878–1915. [493,495]
- Rumelhart, D. E., Hinton, G. E., and Williams, R. J. (1986), “Learning Representations by Back-propagating Errors,” *Nature*, 323, 33–36. [501]
- Unacast (2020), “Unacast Social Distancing Dataset.” <https://www.unacast.com/covid19/social-distancing-scoreboard>. [493]
- von Luxburg, U. (2007), “A Tutorial on Spectral Clustering,” *Statistics and Computing*, 17, 395–416. [493]
- Wang, L. and Wong, A. (2020), “Covid-net: A Tailored Deep Convolutional Neural Network Design for Detection of Covid-19 Cases from Chest X-ray Images,” *Science Reports*, 10, 19549. [493]
- Wasserman, S., and Anderson, C. (1987), “Stochastic a Posteriori Blockmodels: Construction and Assessment,” *Social Networks*, 9, 1 – 36. [492]
- Xie, M., Singh, K., and Strawderman, W. E. (2011), “Confidence Distributions and a Unifying Framework for Meta-Analysis,” *Journal of the American Statistical Association*, 106, 320–333. [505]
- Yang, Z., Zeng, Z., Wang, K., Wong, S.-S., Liang, W., Zanin, M., Liu, P., Cao, X., Gao, Z., Mai, Z., Liang, J., Liu, X., Li, S., Li, Y., Ye, F., Guan, W., Yang, Y., Li, F., and Yuqi Xie, S. L., Liu, B., Wang, Z., Zhang, S., Wang, Y., Zhong, N., and He, J. (2020), “Modified Seir and AI Prediction of the Epidemics Trend of Covid-19 in China Under Public Health Interventions,” *Journal of Thoracic Disease*, 12, 165–174. [493]
- Zheng, C., Deng, X., Fu, Q., Zhou, Q., Feng, J., Ma, H., Liu, W., and Wang, X. (2020), “Deep Learning-based Detection for Covid-19 From Chest CT Using Weak Label,” medRxiv. [493]